Pérez-López, D.; Gasulla Mestre, I.; Capmany Francoy, J.; Sanchez Fandiño, JA.; Muñoz Muñoz, P.; Alavi, H. (2016). Figures of merit for self-beating filtered microwave photonic systems. Optics Express. 24(9):10087-10102. doi:10.1364/OE.24.010087.

Figures of merit for self-beating filtered microwave photonic systems

Daniel Pérez,[1] Ivana Gasulla,[1] José Capmany,*[1] Javier S. Fandiño,[1] Pascual Muñoz,[1] and Hossein Alavi[2]

[1] *ITEAM Research Institute, Universitat Politécnica de Valencia, Camino de Vera s/n, 46022 Valencia, Spain*
[2] *Intel Labs, Hillsboro, OR, USA*
** jcapmany@iteam.upv.es*

Abstract: We present a model to compute the figures of merit of self-beating Microwave Photonics systems, a novel class of systems that work on a self-homodyne fashion by sharing the same laser source for information bearing and local oscillator tasks. General and simplified expressions are given and, as an example, we have consider their application to the design of a tunable RF MWP BS/UE frontend for band selection, based on a Chebyshev Type-II optical filter. The applicability and usefulness of the model are also discussed.

OCIS codes: (060.2360) Fiber optics links and subsystems; (060.5625) Radio frequency photonics; (130.0250) Optoelectronics; (350.4010) Microwaves; (130.3120) Integrated optics devices.

References and links

1. J. Capmany and D. Novak, "Microwave photonics combines two worlds," Nat. Photonics **1**, 316-330 (2007).
2. J. Yao, "Microwave photonics," J. Lightwave Technol. **27**(3), 314-335 (2009).
3. J. E. Mitchell, "Integrated wireless backhaul over optical access networks," J. Lightwave Technol. **32**(20), 3373-3382 (2014).
4. D. Pastor, B. Ortega, J. Capmany, P.Y. Fonjallaz, and M. Popov, "Tunable microwave photonic filter for noise and interference suppression in UMTS base stations," Electron. Lett. **40**, 997-999 (2004)
5. See "Technology focus on Microwave photonics," Nat. Photonics **5**, 723–736 (2011).
6. A. L. Ricchiuti, J. Hervas, D. Barrera, S. Sales, and J. Capmany, "Microwave photonics filtering technique for interrogating a very-weak fiber bragg grating cascade sensor," IEEE Photonics J. **6**(6), 1-10 (2014).
7. D. A. I. Marpaung, C. Roeloffzen, R. Heideman, A. Leinse, S. Sales, and J. Capmany, "Integrated microwave photonics," Laser Photon. Rev. **7**, 506-538 (2013).
8. J. Capmany, J. Mora, I. Gasulla, J. Sancho, J. Lloret, and S. Sales, "Microwave photonic signal processing," J. Lightwave Technol. **31**(4), 571-586 (2013).
9. C. G. H. Roeloffzen, L. Zhuang, C. Taddei, A. Leinse, R. G. Heideman, P. W. L. van Dijk, R. M. Oldenbeuving, D. A. I. Marpaung, M. Burla, and K. J. Boller, "Silicon nitride microwave photonic circuits," Opt. Express **21**(19), 22937-22961 (2013).
10. I. Gasulla and J. Capmany, "Analytical model and figures of merit for filtered microwave photonic links," Opt. Express **19**, 19758-19774 (2011).
11. H. Xie, O. Oliaei, P.Rakers, R. Fernandez, J. Xiang, J. Parkes, J. Riches, R. Verellen, M. Rahman, V. Bhan, and D. B. Schwartz, "Single-Chip Multiband EGPRS and SAW-Less LTE WCDMA CMOS receiver with diversity," IEEE Trans. Microwave Theory Tech. **60**(5), 1390-1396 (2012).
12. C. K. Madsen and J. H. Zhao, *Optical Filter Design and Analysis* (John Wiley & Sons, Inc., 1999).
13. M. S. Rasras, Y-K. Chen, K-Y. Ti, M. P. Earnshaw, F. Pardo, M. A. Cappuzzo, E. Y. Chen, L. T. Gomez, F. Klemens, B. Keller, C. Volle, L. Buhl, J. M. Wyrwas, M. C. Wu, R. Peach, S. Meredith, C. Middleton, and R. DeSalvo, "Reconfigurable linear optical FM discriminator," IEEE Photon. Technology Lett. **24**(20), 1856-1859 (2012).
14. P. Alipour, A. A. Eftekhar, A. H. Atabaki, Q. Li, S. Yegnanarayanan, C. K. Madsen, and A. Adibi, "Fully reconfigurable compact RF photonic filters using high-Q silicon microdisk resonators," Opt. Express **19**, 15899-15907 (2011).
15. S. Ibrahim, N. K. Fontaine, S. S. Djordjevic, B. Guan, T. Su, S. Cheung, R. P. Scott, A. T. Pomerene, L. L. Seaford, C. M. Hill, S. Danziger, Z. Ding, K. Okamoto and S. J. B. Yoo, "Demonstration of a fast-reconfigurable silicon CMOS optical lattice filter," Opt. Express **19**, 13245-13256 (2011).

16. J. S. Fandiño, J. D. Domenech, P.Muñoz, and J. Capmany, "Integrated InP frequency discriminator for phase-modulated microwave photonic links," Opt. Express **21**, 3726–3736 (2013).
17. D. Pérez, I. Gasulla, and J. Capmany, "Software-defined reconfigurable microwave photonics processor," Opt. Express **23**, 14640-14654 (2015)
18. J. Capmany, I. Gasulla and D. Pérez, "Microwave Photonics: The programmable processor," Nat. Photonics **10**(1), 6-8 (2016).
19. W. Liu, M. Li, R. S. Guzzon, E. J. Norberg, J. S. Parker, M. Lu, L.A. Coldren, and J. Yao, "A fully reconfigurable photonic integrated processor," Nat. Photonics **10**(2), 190-196 (2016).
20. C.K. Madsen, "Efficient architectures for exactly realizing optical filters with optimum bandpass designs," IEEE Photon. Technol. Lett. **10**, 1136–1138 (1998).
21. P. A. Besse, E. Gini, M. Bachmann, and H. Melchior, "New 2×2 and 1×3 Multimode Interference Couplers with Free Selection of Power Splitting Ratios," J. Lightw. Technol. **14**(10), 2286–2293 (1996).

1. Introduction

Microwave photonics (MWP) [1,2], is expected to extend its use in the next years to novel emerging information technology scenarios, such as 5G mobile communications [3,4] internet of the things (IoT) [5] and sensing [6]. These application fields require technical approaches capable of smoothly interfacing the wireless and fibre segments of communication networks. MWP is the best positioned technology to achieve this target. However, the successful accomplishment of this objective relies on the possibility of implementing agile and reconfigurable MWP subsystems, featuring broadband operation and low Space, Weight and Power (SWaP) metrics. A solution to the above restrictions is resorting to integrated microwave photonics [7,8], where complex MWP systems are integrated on a single chip. Furthermore, the possibility of evolving from pure intensity modulated and direct detection (IM-DD) configurations to more advanced coherent or self-coherent detection schemes, allowing for more complex modulation formats, is a highly desirable feature.

An emerging and important class of MWP systems operates in the so-called self-beating mode. In this scheme, shown in Fig. 1, a continuous wave (CW) optical carrier is first split into two paths by an input coupler characterized by a coupling coefficient K_1. The CW carrier in one of the paths is modulated (either single or double sideband) by an input radiofrequency (RF) signal in an external modulator, filtered to supress the optical carrier leaving the single (or double) RF sideband(s), which is (are) then processed by an optical core represented by a field transfer function $H(\omega)$. In the other arm, the CW signal propagates subject to no modulation. Both paths are finally combined by an output coupler characterized by a coupling coefficient K_2 prior to enter to one (or two) photodetector(s), where the RF-modulated signal beats with the CW signal that actually operates as a self local oscillator. In essence, this operation corresponds to a self-homodyne coherent system that is called to play a significant role in on-chip tunable MWP signal processors. In particular, this approach has been recently shown to bring unprecedented flexibility in integrated MWP filters and beamforming networks [9]. As with any MWP system, the performance of self-beating configurations can be described in terms of the traditional figures of merit [10]: RF Gain, Noise Figure (NF) and Spurious Free Dynamic Range (SFDR). However, to our knowledge, there is no reported model yielding expressions for these figures in this particular, but important case. The purpose of this paper is to report such model. In fact, the original contribution of this paper is to derive the expression for the contribution from the signal-local oscillator beating term, which is not applicable to the case described in [10] and which will dominate the figures of merit in practice. We consider amplitude modulation in two different system configurations: single and balanced detection respectively. Section 2 develops the general model that takes into account the impact of most of the factors behind non-ideal operation (insertion losses, finite CW optical carrier suppression, polarization mismatch, etc.). This is followed by the simplified expressions corresponding to the case where the self-beating term after detection dominates over the direct detection term. In section 3 we apply the model to a specific, but important example, corresponding to a reconfigurable front end based on an integrated tunable

bandpass MWP filter. Results are provided for the two cases and a discussion on the model applicability and usefulness is provided. Section 4 summarizes and concludes the paper.

2. Self-beating Filtered MWP system with amplitude modulation

2.1 Figures of Merit definitions

The figures of merit of a MWP link are given by the end-to-end RF gain, the Noise Figure and the Dynamic Range. The end-to-end RF gain (or loss) of the self-beating MWP link represented in Fig. 1 is defined as the ratio of the RF power (at the modulating angular frequency Ω) delivered to a matched load at the photodetector output $P_{RF}|_{out}$ to the available RF power at the input (at the modulating angular frequency Ω), $P_{RF}|_{in}$, delivered to the modulation device. In other words, $G_{RF} = P_{RF}|_{out}(\Omega) / P_{RF}|_{in}(\Omega)$, being $P_{RF}|_{in}(\Omega) = V_{rf}^2/(2Z_{in})$,where V_{rf} is the amplitude of the voltage signal applied to the external modulator and Z_{in} the input impedance. The evaluation of the microwave signal degradation due to noise sources is accounted by the noise figure parameter defined as $NF = N_{tot} / (G_{RF} N_{in})$, where N_{tot} and N_{in} are, respectively, the total ouput and input noise spectral densities. The NF will be referred to the total relative intensity noise parameter (RIN_{tot}), defined as $RIN_{tot} = N_{tot} / (I|_{dc}^2 Z_{out})$, where $I|_{dc}$ represents the DC photocurrent and Z_{out} is the system's ouput impedance. The value of RIN_{tot} has been derived taking into accounte the input and output thermal noises, the shot noise at the detector and the laser noise contributions: $RIN_{tot} = RIN_{i,th} + RIN_{o,th} + RIN_{shot} + RIN_{laser}$. Finally, the figure of merit that characterizes the performance in terms of dynamic range is the spurious free dynamic range (*SFDR*). It is employed to qualify the linearity of microwave devices, analogue-to-digital converters, leser diodes and external modulators. The *SFDR* is defined as the carrier-to-noise ratio when the noise floor in the signal bandwidth equals the power of a given order intermodulation product. The *SFDR* of a link limited by second (IMD_2) or third-order (IMD_3) intermodulation distortion can be computed, respectivel,y from the expressions $SFDR_2 = (OIP_2 / N_{tot})^{1/2}$ or $SFDR_3 = (OIP_3 / N_{tot})^{1/3}$, where OIP_2 and OIP_3 are the linearly extrapolated input RF powers at which the fundamental and, respectively the IMD_2 and IMD_3 output powers become equal.

2.2 General expressions of the Figures of Merit

Figure 1 shows the layout of a general self-beating filtered MWP system with amplitude modulation, the operation principle of which has been described in section 1. We consider in Fig. 1 both balanced detection and ~~direct~~ single detection schemes, the latter being illustrated in the upper right inset. The CW optical source emits an optical power P_o at an angular frequency ω_b. The modulating signal is described by a voltage $V_{RF,in}(t) = V_{dc}+V_{rf} \sin(\Omega_1 t)$ applied to the modulator across an input impedance Z_{in}. V_{dc} is a constant (DC) part that is employed to bias the modulator, while V_{rf} describes the amplitude of the time-varying RF sinusoidal signal of angular frequency Ω_1. The modulator action over the input CW optical signal is described by means of a sinoidal law (Eq. (1) in [10]) and its half-wave voltage V_π. The relevant normalized parameters are $\phi_{rf} = \pi V_{rf}/V_\pi$ and $\phi_{dc} = \pi V_{dc}/V_\pi$. The modulated signal propagates through the upper path, where it is processed by one or several filters characterized by a lumped frequency response $H(\omega)$ and experiences an overall loss characterized by a lumped optical power transmission factor α_U. The CW signal in the lower path is not modulated and experiences an overall loss characterized by a lumped optical power transmission factor α_L. The signals from both paths are combined at coupler K_2 before being detected by either a balanced detection or a direct detection scheme. The balanced configuration comprises two photodetectors placed at each output of the coupler K_2, where each one is characterized by a responsivity $\Re$. The photocurrents generated at each one of these photodetectors are electrically subtracted to produce an output photocurrent $i_{RF,out}(t)$ flowing across an output impedance Z_{out}. The single ~~direct~~ detection scheme comprises one

single detector as shown in the upper right inset of Fig. 1. The detailed derivation of $i_{RF,out}(t)$ and the figures of merit is provided in the Appendix.

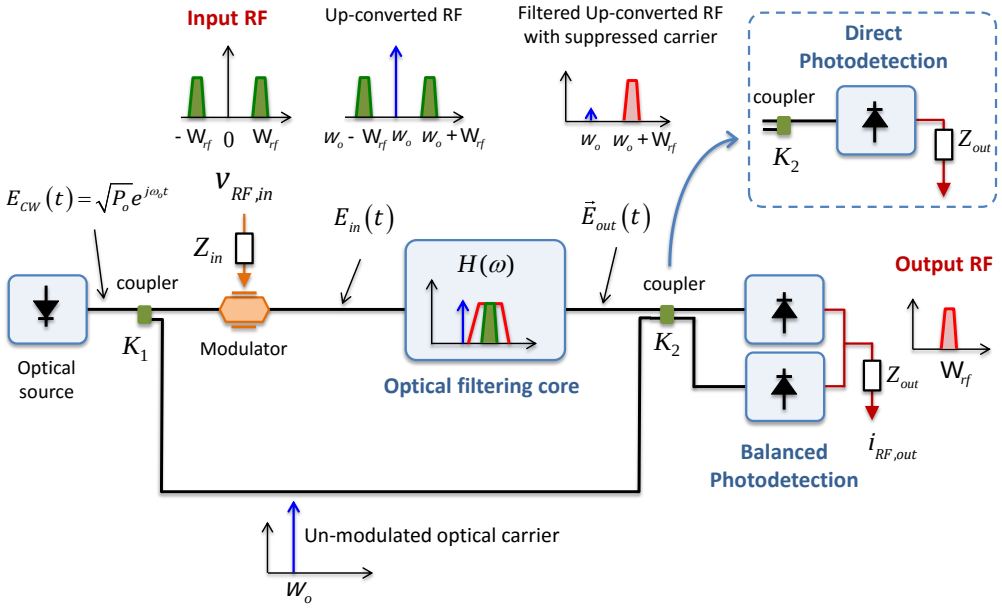

Fig. 1. Layout of a general self-beating filtered MWP system.

To obtain the expressions for the figures of merit of a general layout that applies to both single and balanced detection, we introduce in the Appendix a set of parameters {*C*, *D*, *X*, *Y*} that account for the splitting action of the input and output couplers as well as the optical losses of the upper and lower branches. Following a similar procedure as that reported in [10] we get the main figures of merit as:

$$G_{RF}(\Omega_1)=\frac{P_{RF}^{out}(\Omega_1)}{P_{RF}^{in}(\Omega_1)}=\left[\frac{I_{dc}\pi\sin(\phi_{DC})}{2V_\pi}\frac{D}{X}\right]^2\left|jDA_{\Omega_1}^{I}+CA_{\Omega_1}^{I,B}\right|^2 Z_{in}Z_{out}, \tag{1}$$

$$NF=\frac{RIN_{Total}I_{dc,Total}Z_{out}}{G_{RF}(\Omega_1)k_BT}, \tag{2}$$

$$\begin{aligned}RIN_{Total}&=RIN_{thermal,input}+RIN_{thermal,output}+RIN_{shot}+RIN_{laser}=\\&k_BT\left[\frac{\rho\sin(f_{DC})}{2V_p}\right]^2\left|jDA_{W_1}^{I}+CA_{W_1}^{I,B}\right|^2 Z_{in}+\frac{2k_BT}{\left(\frac{DI_{dc}}{X}\right)^2}Z_{out}\\&=\frac{}{\left[(-1)^p D\left|H(w_o)\right|^2(1-\cos f_{DC})+Y+4C\sin\left(\frac{f_{DC}}{2}\right)\cos j\ \mathrm{Im}\{H(w_o)\}\right]^2}+\\&+\frac{2e}{\left(\frac{DI_{dc}}{X}\right)\left[(-1)^p D\left|H(w_o)\right|^2(1-\cos f_{DC})+Y+4C\sin\left(\frac{f_{DC}}{2}\right)\cos j\ \mathrm{Im}\{H(w_o)\}\right]}+\\&+RIN_{laser}\end{aligned} \tag{3}$$

$$OIP_2 = 2\left(I_{dc} \sin^2\left(\phi_{DC}\right) \frac{D}{X} \right)^2 Z_{out} \frac{\left| jDA^{I}_{\Omega_1} + CA^{I,B}_{\Omega_1} \right|^4}{\left| jDA^{I}_{\Omega_1-\Omega_2} + CA^{I,B}_{\Omega_1-\Omega_2} \right|^2}, \quad (4)$$

$$OIP_3 = 2\left(I_{dc} \sin\left(\phi_{DC}\right) \frac{D}{X} \right)^2 Z_{out} \frac{\left| jDA^{I}_{\Omega_1} + CA^{I,B}_{\Omega_1} \right|^3}{\left| jDA^{I}_{2\Omega_1-\Omega_2} - CA^{I,B}_{2\Omega_1-\Omega_2} \right|}, \quad (5)$$

$$SFDR_2 = \left[\frac{OIP_2}{N^{\text{output}}_{\text{Total}}} \right]^{\frac{1}{2}}, \qquad SFDR_3 = \left[\frac{OIP_3}{N^{\text{output}}_{\text{Total}}} \right]^{\frac{2}{3}}, \quad (6)$$

In Eq. (1)-(6), $G_{RF}(\Omega_1)$ represents the RF gain, NF the overall noise figure that depends on the total output noise N_{Total}, while OIP_2 and OIP_3 represent the second and third optical interception points that are needed, respectively, to compute the second- and third-order Spurious Free Dynamic Ranges. The polarization mismatch between the beating optical signals from the upper and lower branches is given by $cos\varphi$, $I_{dc} = \Re P_o/2$ and $A^{I}_{\Omega_1}$, $A^{I}_{\Omega_1-\Omega_2}$ and $A^{I}_{2\Omega_1-\Omega_2}$ are the spectral coefficients respectively for the fundamental, second- and third-order intermodulation terms for intensity modulated direct detection MWP systems that are defined in [10]. Also, note that $N^{\text{output}}_{total} = RIN_{Total} I^2_{dc,Total} Z_{out}$. Finally, $A^{I,B}_{\Omega_1}$, $A^{I,B}_{\Omega_1-\Omega_2}$ and $A^{I,B}_{2\Omega_1-\Omega_2}$ are the spectral coefficients respectively for the fundamental, second- and third-order intermodulation terms for the beating contribution given in the Appendix.

2.3 Simplified expressions

Equations (1)-(6) provide the most general expressions for the computation of the figures of merit, taking into account most of the factors behind non-ideal operation (insertion losses, finite CW optical carrier suppression, non-ideal filtering effects, polarization mismatch, etc.). In practice however several simplifications can be made. The most important one is that the term from the beating of the CW carrier (lower branch) and the modulated signal (upper branch) should be the dominant one in the output photocurrent. We will also assume that the optical carrier is completely suppressed by the filter in the upper branch, as illustrated in the upper part of Fig. 1. Under these conditions, the general figures of merit from Eq. (1),(3),(4) and (5) simplify to:

$$G_{RF}\left(\Omega_1\right) = \left[\frac{I_{dc}\pi \sin\left(\phi_{DC}\right)}{2V_{\pi}} \frac{CD}{X} \left| A^{I,B}_{\Omega_1} \right| \right]^2 Z_{in} Z_{out}, \quad (7)$$

$$N^{\text{output}}_{\text{Total}} = 2^p k_B T + 2eI_{dc} Z_{out} \frac{DY}{X} + \left[\frac{I_{dc} p \sin\left(f_{DC}\right)}{2V_p} \frac{CD}{X} \left| A^{I,B}_{\Omega_1} \right| \right]^2 Z_{in} Z_{out} k_B T, \quad (8)$$

$$OIP_2 = 2\left(I_{dc} \sin^2\left(\phi_{DC}\right) \frac{CD}{X} \right)^2 Z_{out} \frac{\left| A^{I,B}_{\Omega_1} \right|^4}{\left| A^{I,B}_{\Omega_1-\Omega_2} \right|^2}, \quad (9)$$

$$OIP_3 = 2\left(I_{dc} \sin\left(\phi_{DC}\right) \frac{CD}{X} \right)^2 Z_{out} \frac{\left| A_{\Omega_1}^{I,B} \right|^3}{\left| A_{2\Omega_1-\Omega_2}^{I,B} \right|}. \quad (10)$$

Note that the noise figure and the spurious free dynamic ranges are obtained substituting Eq. (8)-(11) into Eq. (2) and (6), respectively. In the case of balanced detection, we consider in addition ideal operation, that is, the same responsivity in both photodetectors and $K_2 = 1/2$ that results in $CD/X = \sqrt{a_U a_L K_1 \left(1 - K_1\right)}$ and $DY/X = 0$.

3. Application example, results and discussion

3.1 MWP Tunable duplexer

Manufacturers of RF front ends are currently facing the increasingly difficult problem of designing and producing tunable multi-band systems, while still providing acceptable performance, compact footprint and a reduced power consumption [11]. Fig. 2 shows a schematic diagram of a typical Base Station (BS)/User Equipment (UE), where the RF front-end section has been conveniently highlighted.

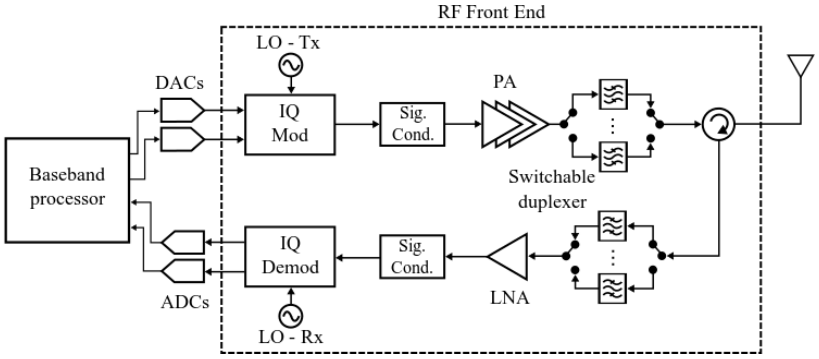

Fig. 2. Diagram of a typical BS/UE radio interface. The RF front end is enclosed with a discontinuous line.

Located between the baseband digital processor and the antenna, RF front ends encompass a series of critical components for the correct operation of the system, including signal conditioning, high-power amplifiers and duplexers. As we can see, the capability of the device to switch among different bands basically depends on the tunability of the duplexer, which is located just before the antenna to both filter and isolate the transmitter and receiver channels. Tunability is achieved by means of internally switched RF paths that drive different duplexers. However, this parallel approach will be put under significant strain as the increasing number of bands leads to increased design complexities and chip sizes. Thus, new and disrupting solutions for the design of tunable and versatile duplexers become mandatory for the development of future wireless communication systems.

The use of integrated microwave photonic technologies has been proposed to tackle this challenging problem, [7]. Figure 3 depicts a basic diagram of a tunable MWP duplexer that we will consider as an application example. The operation principle can be described as follows. First, a tunable laser (TL) acts as the self-local oscillator (LO) of both the transmitter and the receiver, serving as an optical carrier where the RF waveform is encoded via electro-optic/electro-absorption modulators. The optical signal is then filtered with a reconfigurable optical filter that independently selects the RF bands of interest, both in transmission and reception. Finally, respective photodiodes recover the RF signal back from the optical domain, which is then either radiated by the antenna or used to drive a low-noise amplifier further down the receiver chain.

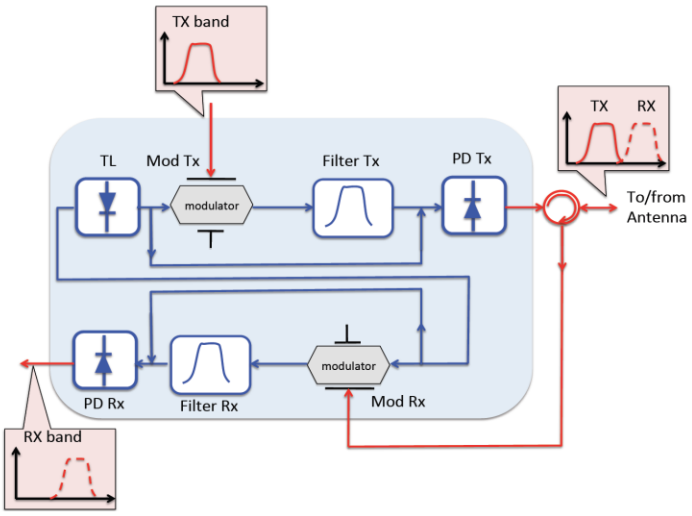

Fig. 3. Schematic diagram of a microwave photonic duplexer.

In this photonic approach, the tunability of the duplexer relies on the reconfigurability of the integrated optical filters, whose transfer functions can be indeed completely modified with either thermo-optic or electro-optic phase modulators [12]. This is possible because integrated optical filters are made of a concatenation of more basic elements, such as microring resonators and Mach-Zehnder interferometers (MZIs), which exploit the coherence interference between different optical waves to achieve the desired transfer function. In simple terms, light is basically split into many different paths that are then recombined to achieve the desired interference at a given frequency range. However, unlike in electronics and RF, broadband reconfigurable couplers and phase-shifting elements are straightforward to implement in photonic integrated circuits by exploiting the aforementioned physical effects [13-15], which only require an external supply of DC voltage/current to operate.

3.2 Optical filter description

As an application example for the above described model, we consider a band duplexer employing a tunable integrated filter composed of a ring-loaded Mach-Zehnder interferometer [16], as shown in the upper part of Fig. 4. This type of filter is made of a symmetric MZI, where both interferometer arms are coupled to a set of ring resonators of the same perimeter. The coupling between the top/bottom MZI arms and the ring resonators is achieved by means of optical couplers with different coupling constants. These are schematically shown in upper part of Fig. 4 as $K_{b,i}$ and $K_{t,i}$ (with i = 1, 2), where 'K' stands for the power coupling constant (in linear units), and 'b' and 't' stand for 'bottom' and 'top', respectively. Together with the relative optical phases of the ring resonators ($\phi_{b,i}$, $\phi_{t,i}$) and the relative phases of the MZI arms ($\phi_{t,a}$, $\phi_{b,a}$), they completely define the transfer function of the filter, as described in [20].

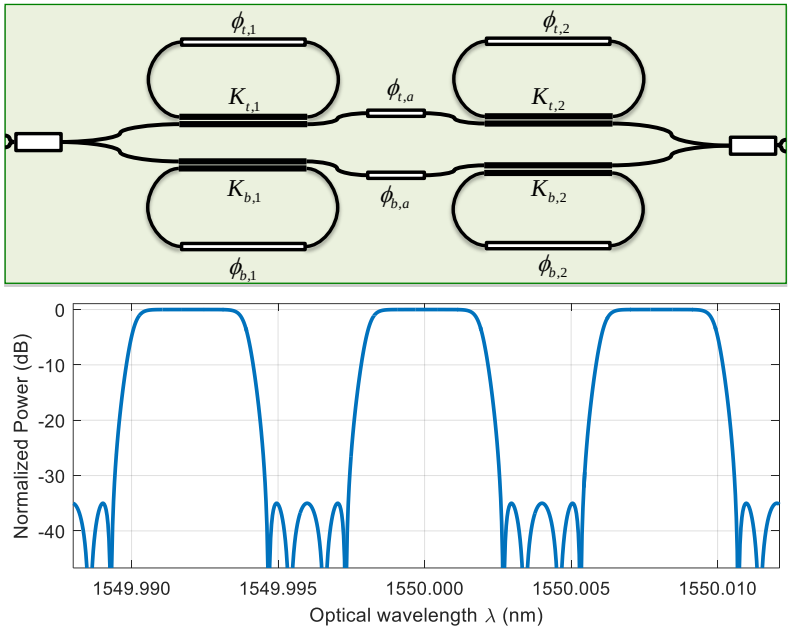

Fig. 4. (Upper) Schematic diagram of a ring-loaded Mach-Zehnder Interferometer considered as an example. (Lower) Chebyshef Type-II filter implemented by the ring-loaded MZI (filter details in text).

Ring-loaded MZI filters can be mathematically described with the same formalism employed in digital signal processing filters [12], so identical techniques can be used for their design. Our structure implements a canonical, 4th-order Chebyshev Type-II filter with a low-pass response. It features a stopband rejection of 35 dB and a passband cutoff frequency of 9.44 GHz. The designed filter is shown in the lower part of Fig. 4. The values of the different phase shifts and coupling constants required to achieve this transfer function are: $K_{t,1} = K_{b,1} =$ 0.489, $K_{t,2} = K_{b,2} =$ 0.943, $\phi_{t,1} = -\phi_{b,1} =$ 86.1096º, $\phi_{t,2} = -\phi_{b,2} =$ -98.7306º, and $\phi_{t,a} = -\phi_{b,a} =$ 54.5716º. Also note that the optical response of the filter is periodic in frequency. The spectral period is known as the Free Spectral Range (FSR), and in this case is 20 GHz.

The integrated filter was designed to be implemented in an InP platform at a nominal wavelength of 1550 nm. The effective group index of the employed waveguides is 3.7056, which yields a ring perimeter of 4.0451 mm for a FSR of 20 GHz. Multimode interference couplers (MMIs) were employed to implement the input/output 3-dB couplers that split/recombine the signals in the MZI arms, as well as the couplers with different coupling constants that connect the arms with the ring resonators. The latter were obtained by tapering the width of the multimode waveguides, following the procedure described in [21].

3.3 Results for single detection

We have applied the model derived in section 2 to a single-detector RF front-end configuration using the optical filter described in subsection 3.2. We consider single-sideband modulation with a high degree of optical carrier suppression (around 35 dB achieved as compared to the selected RF bands) by appliying a carrier frequency shifting of $\Delta f_0 =$ 10 GHz. For the evaluation of the figures of merit we have employed the general version of the model, i.e. Eqs. (1)-(7), and the following values for the relevant parameters: $\alpha_L = 10^{-3/10}$, $\varphi = 0$, (perfect state of polarization matching), $\phi_{dc} = \pi/2$ (MZM biased at the quadrature point), $V_\pi =$ 6.9 volt (typical values range between 3 and 9 volt), $I_{dc} =$ 5 mA, , $T =$ 298 ºK, $k_B =$ 1.3810^{-23} J ºK^{-1}, $K_1 = K_2$, $Z_{in} = Z_{out} =$ 50 Ω. For the signal frequencies we have chosen (referred to the value of the optical carrier frequency $f_o = 2\pi\omega_o$), $f_1 = 2\pi\Omega_1 =$ 6.5 GHz, $f_2 = 2\pi\Omega_2 =$ 6.6 GHz, $|f_1 - f_2| =$ 100 MHz (for second-order intermodulation products) and $|2f_1 - f_2| =$ 6.4 GHz, $|2f_2 -$

f_1| = 6.7 GHz, (for third-order intermodulation products). Figure 5 displays the RF link gain (RF filter response) for the optimum case $\alpha_U = \alpha_L$ as a function of the frequency. The locations of the relevant RF tones are also displayed. As we can observe, the spectral characteristic of the optical filter in Fig. 4 (Chebyshev Type-II) has been perfectly translated or downconverted into the RF domain. In Fig. 6 we represent the contour plots for the RF gain, the noise figure and the second- and third-order spurious free dynamic ranges as a function of K_1 and K_2 for a realistic case where α_L = 3 dB and α_U = 6 dB (note that, due to the presence of the modulator and the optical filter in the upper branch, it is reasonable to assume that $\alpha_L < \alpha_U$). As we can see, the $K_1 = K_2$ direction defines a region for optimum operation for all these performance parameters. For this particular case, we represent in Fig. 7 the values of the RF gain, Noise Figure, $SFRD_2$ and $SFDR_3$, where the loss value of the upper branch α_U is taken as a parameter.

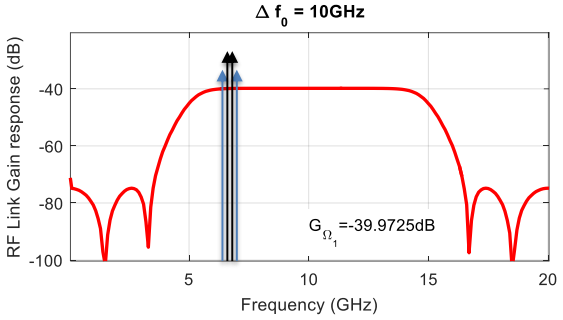

Fig. 5. RF frequency response of the RF-Front end obtained by self-beating and single detection.

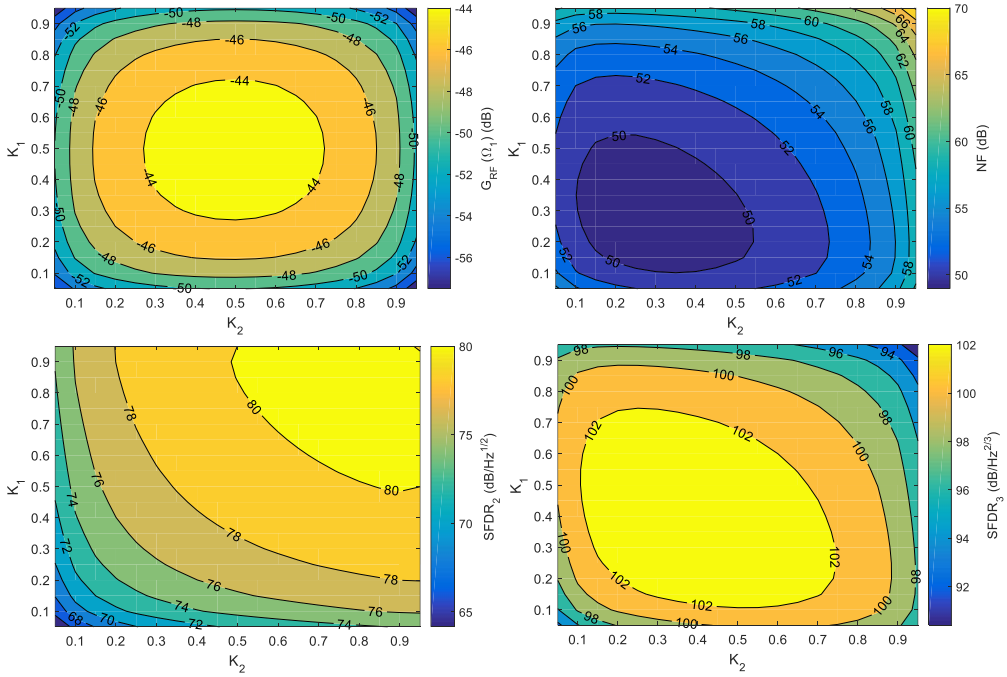

Fig. 6. Contour plots vs the value of K_1 and K_2 for the RF Gain (upper left), Noise Figure (upper right), $SFDR_2$ (lower left) and $SFDR_3$ (lower right) for the tunable RF-front end obtained by self-beating and single detection. System parameters are given in the text with α_L = 3 dB and α_U = 6 dB.

The front-end performance is very sensitive to the loss in the two branches. As we can observe from Fig. 7, it impacts three of the four figures of merit and the best values are obtained when $\alpha_U = \alpha_L$. However, as we have previously explained, it is realistic to assume that in practice $\alpha_U > \alpha_L$. Note that the best values for each figure of merit are obtained for different values of $K = K_1 = K_2$. In particular, the region around $K = 0.5$ renders optimum values for the RF Gain and $SFDR_3$, and almost optimum for $SDFR_2$ and NF. Since $SDFR_2$ is not relevant for suboctave frequency spanning systems and the NF value is only 1 dB above the minimum, we conclude that $K = 0.5$ is the best operating point for this kind of configuration.

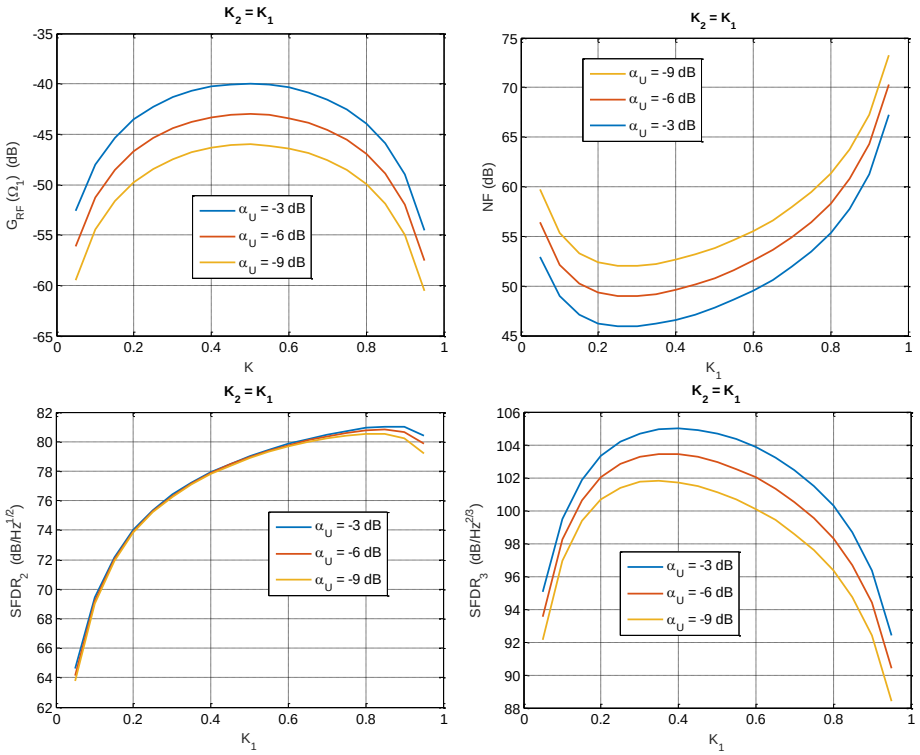

Fig. 7. RF Gain (upper left), Noise Figure (upper right), Second-order Spurious free dynamic range (lower left) and Third-order Spurious free dynamic range (lower right) vs the value of the couplers $K_1 = K_2 = K$, taking α_U as a parameter for the tunable RF-front end obtained by self-beating and single detection. System parameters are given in the text.

3.4 Results for balanced detection

In this case we combine the two photocurrents generated by the two outputs from the output coupler. We expect an improved performance in terms of optimum RF gain as well as in terms of noise figure due to the common mode noise rejection under balanced detection. We use the same values for the rest of the system parameters as in the single detection case.

Figure 8 displays the RF link gain (RF filter response) for the optimum case, $K_2 = 0.5$, and $\alpha_U = \alpha_L$ as a function of the frequency. The location of the relevant RF tones are also displayed and, again, for comparison single-sideband modulation with optical carrier suppression is considered. As in the single-detector case, the spectral characteristic of the optical filter (Chebyshev Type-II) has been perfectly translated or downconverted into the RF domain. Note that the optimum gain in this case is 6 dB higher as the detected RF current is double as compared to the single-detector case (i.e. RF power is 4 times higher). In this case, the requirement for balanced detection directly implies that K_2 should be as close as possible

to 0.5. Nevertheless, and as in subsection 3.3, we show in Fig. 9 the contour plots for the RF gain, the noise figure and the second- and third-order spurious free dynamic ranges as a function of K_1 and K_2. Again, we consider a realistic case where α_L = 3 dB and α_U = 6 dB.

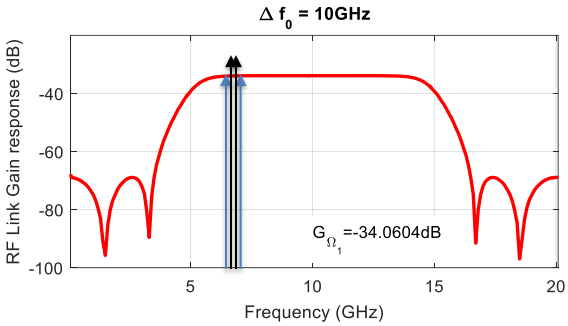

Fig. 8. RF frequency response of the RF-Front end obtained by self-beating and optimum balanced detection (K_2 = 0.5).

As we can observe once more, the $K_1 = K_2$ direction defines a region for optimum operation for most of the performance parameters. For this particular case, we represent in Fig. 10 the values of the RF gain, Noise Figure, $SFRD_2$ and $SFDR_3$. In this last figure the loss value of the upper branch α_U is taken as a parameter.

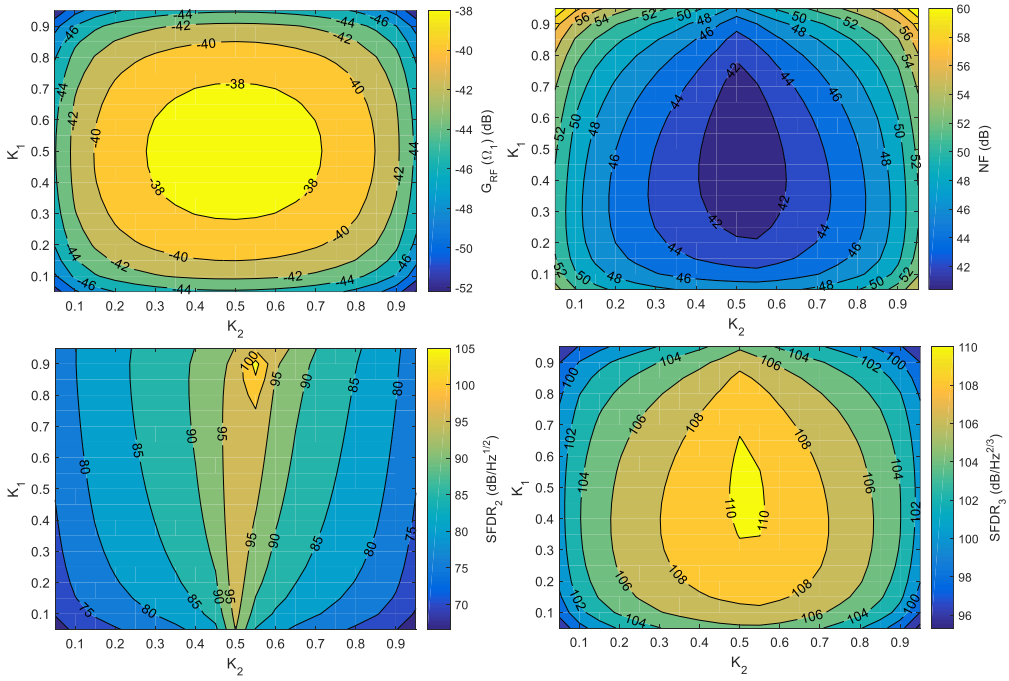

Fig. 9. Contour plots vs the value of K_1 and K_2 for the RF Gain (upper left), Noise Figure (upper right), $SFDR_2$ (lower left) and $SFDR_3$ (lower right) for the tunable RF-front end obtained by self-beating and balanced detection. System parameters are given in the text with α_L = 3 dB and α_U = 6 dB.

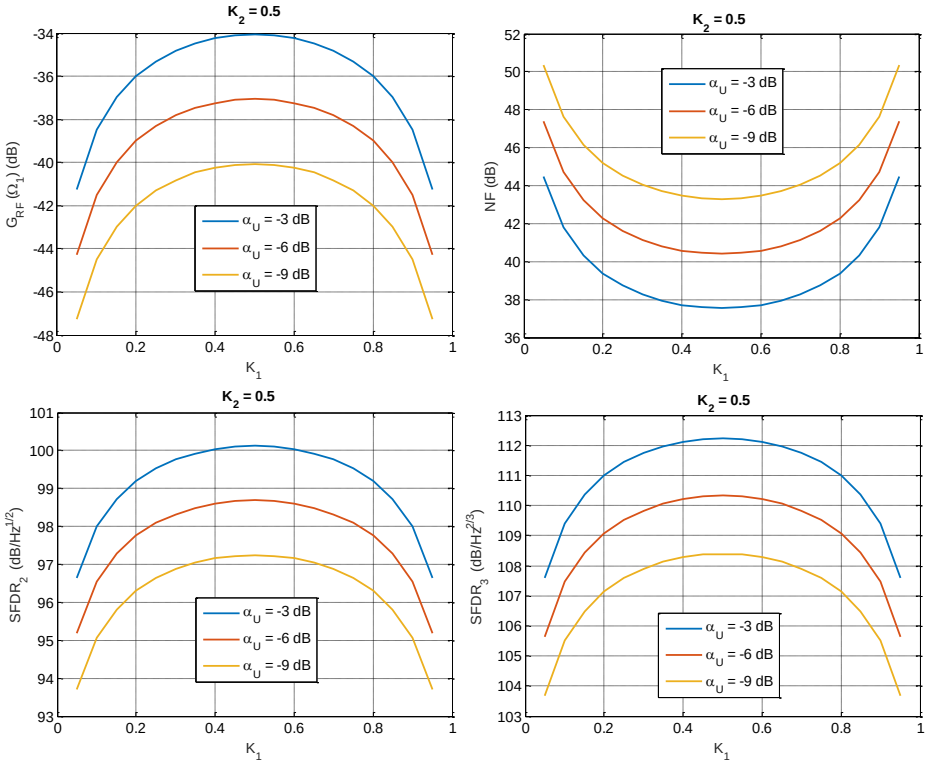

Fig. 10. RF Gain (upper left), Noise Figure (upper right), $SFDR_2$ (lower left) and $SFDR_3$ (lower right) vs the value of the input coupler K_1 and taking α_U as a parameter for the tunable RF-front end obtained by self-beating and balanced detection ($K_2 = 0.5$).

As in the single-detection case, the front-end performance is very sensitive to the loss in the two branches. In this case, however, it impacts all the four figures of merit and the best values are obtained when $\alpha_U = \alpha_L$. However, as mentioned before, it is realistic to assume that in practice $\alpha_U > \alpha_L$. Another difference is the symmetric behaviour of all the figures of merit around the point $K_1 = 0.5$. We therefore conclude that $K_1 = K_2 = 0.5$ is the best operating point for this kind of configuration.

3.5 Discussion

The model developed in section 2 is very useful for two main reasons. In first place, it provides a means for the computation of the figures of merit in a novel class of MWP systems, which is called to play a significant role in integrated optic chips and particularly in programmable processors [17-19]. Self-beating MWP configurations using OSSB modulation are ideal for small footprint subsystems, where a common laser source can be employed both as an optical source for modulation as well as a self local oscillator, opening a completely new class of operation regime, where optical field spectral characteristics are directly translated into the RF region. In our case, the general model accounts for a considerable list of parameters that influence the overall performance. Furthermore, the simplified model can be directly applied to many practical situations where the term from the beating of the CW carrier and the modulated signal should dominated in the output photocurrent, i.e. $C > D$.

A second added value of the model is that it can be employed as a tool for comparing different configurations of complex MWP systems designed to perform the same task and to choose the best option in terms of the standard performance metrics given by the figures of merit. In this context, in the example developed in sections 3.3 and 3.4, the model provides

relevant information to compare both approaches. For instance, it provides the optimum operation conditions as far as the values of the coupling constants K_1 and K_2 are concerned. For both configurations, the ideal performance is achieved around the $K_1 = K_2 = 0.5$ region, however the performance of each one is completely different. While the single-detector architecture shows a completely asymmetric performance around this point, the balanced-detector configuration results in a symmetric performance and is, therefore, more robust against drifts in the value of the coupling constants. For equal parameters, the balanced configuration renders a higher RF Gain (by 6 dB), higher $SDFR_2$ (by 19 dB) and $SDFR_3$ (by 7 dB) and lower NF (by 7 dB) compared to the single-detection case.

The model allows as well to analyze the performance of a given configuration when one or several relevant parameters (losses, DC modulator biasing, V_π, etc.) are changed, providing an invaluable help in the design and performance prediction stages.

4. Summary and conclusions

We have presented a model to compute the figures of merit of self-beating MWP systems, a novel class which is called to play a principal role in novel integrated MWP circuits for emerging applications, such as 5G, IoT and sensing. This category of systems work on a self-homodyne fashion by sharing the same laser source for information bearing and local oscillator tasks. The reduced footprint of photonic chips makes this configuration highly desirable as less components are required, and optical filtering and other complex functionalities can be directly translated into the RF domain.

The expressions developed are general but can be simplified in many practical cases. As an example, we have considered their application to the design of a tunable RF MWP BS/UE frontend for band selection, based on a Chebyshev Type-II optical filter. We have employed the model to compare two possible designs, a single-detector and a balanced-detector configuration, providing useful information in the search of the optimum operation points and also in the comparison of both designs. The applicability and usefulness of the model has been also discussed.

Appendix: Detailed Derivation of $i_{RF,out}(t)$ and the figures of Merit

We consider the self-beating MWP link shown in Fig.1. Referring to this figure, the system parameters given in section 2.2 and the vector field at the output of the upper link $\mathbf{E}_{out}(t)$, the output photocurrent can be computed yielding:

$$\begin{aligned} i_{RF,out}(t) &= \Re(2K_2-1)\left|E_{out}(t)\right|^2 - \Re(2K_2-1)\alpha_L K_1 P_o + 2\Re\sqrt{K_1K_2(1-K_2)\alpha_L P_o}\,e^{-j\omega_o t}\vec{E}_{out}(t).\vec{\mathbf{e}}_d + \\ &+ 2\Re\sqrt{K_1K_2(1-K_2)\alpha_L P_o}\,e^{j\omega_o t}\vec{E}^*_{out}(t).\vec{\mathbf{e}}_d = i_{dd}(t) + i_b(t), \end{aligned} \tag{11}$$

where $\mathbf{e}_d$ is the vector representing the sate of polarization of the CW laser. The first term in (12) is $i_{dd}(t)$, the contribution due to direct detection and its impact over the figures of merit has been evaluated in [10]. Although, in principle, this contribution has to be taken into account in the derivations, in practice it is the second and third terms that correspond to the beating between the signal and local oscillator $i_b(t)$ which is expected to dominate in their overall value. The derivation of the impact of this term is original from this paper.

The action of the modulator is described in the time and frequency domains by [10]:

$$
\begin{aligned}
&E_{out}\big|_{MZM}(t) = j\sqrt{\alpha_{MZM}}E_{in}(t)\sin\left[\phi_{dc} + (\phi_{rf}/2)\sin\Omega t\right],\\
&E_{out}\big|_{MZM}(\omega) = 2\pi\sqrt{\alpha_{MZM}}\sum_{n=-\infty}^{\infty} B_n J_n(\phi_{rf}/2)E_{in}(\omega - n\Omega),\\
&B_n = (-1)^n j^{|n|+1}\sin(\phi_{dc}/2 + |n|\pi/2),
\end{aligned}
\tag{12}
$$

where B_n are the spectral coefficients of the modulator. Introducing (12) in (11) and taking into account that $\boldsymbol{E}_{out}(\omega) = H(\omega)\,\boldsymbol{E}_{out}|_{MZM}(\omega)$, we have after a straightforward but lengthy calculation:

$$
\begin{aligned}
&i_b(t) = \{\vec{\mathbf{e}}_u.\vec{\mathbf{e}}_d = \cos\varphi\} =\\
&= 2\Re P_o\sqrt{K_1K_2(1-K_2)(1-K_1)\alpha_L\alpha_U}\\
&\sum_{n=-\infty}^{\infty}\sum_{k=-\infty}^{\infty} J_{|n|}\left(\frac{\phi_{RF}}{2}\right)J_{|k|}\left(\frac{\phi_{RF}}{2}\right)\left[B_{n,k}H(\omega_o + n\Omega_1 + k\Omega_2) + (-1)^{|n|+|k|}B^*_{-n,-k}H^*(\omega_o - n\Omega_1 - k\Omega_2)\right]e^{j(n\Omega_1+k\Omega_2)t}\cos\varphi.
\end{aligned}
\tag{13}
$$

Equation (13) provides the value of the linear and intermodulation terms required for the computation of the contribution of the self-beating current to the Figures of merit of the MWP link. In combination with equation (6) of [10], they provide the overall output current. For example, under small signal modulation approach, the phasor for the fundamental RF photocurrent at Ω_1 is given by:

$$
\begin{aligned}
&\hat{I}(\Omega_1) = \hat{I}_{dd}(\Omega_1) + \hat{I}_b(\Omega_1) =\\
&= I_{dc}\sqrt{\alpha_U(1-K_1)}\left(\frac{\phi_{RF}}{4}\right)\sin(\phi_{DC})\left[2\sqrt{K_1K_2(1-K_2)\alpha_L}A^{I,B}_{\Omega_1} - j(2K_2-1)\sqrt{\alpha_U(1-K_1)}A^{I}_{\Omega_1}\right],
\end{aligned}
\tag{14}
$$

where:

$$
A^{I,B}_{\Omega_1} = \frac{\left[H(\omega_o + \Omega_1) - H^*(\omega_o - \Omega_1)\right]}{\sin(f_{dc}/2)}\cos j
\tag{15}
$$

and $A^{I}_{\Omega_1}$, is the spectral coefficient for the fundamental, terms for intensity modulated direct detection filtered MWP systems that defined in [10]. In the same way, the phasors for the second- and third-order RF intermodulation terms are given by:

$$
\begin{aligned}
&\hat{I}(\Omega_1 - \Omega_2) = \hat{I}_{dd}(\Omega_1 - \Omega_2) + \hat{I}_d(\Omega_1 - \Omega_2) =\\
&= I_{dc}\sqrt{(1-K_1)\alpha_U}\left(\frac{\phi_{RF}}{4}\right)^2\left[\sqrt{(1-K_1)\alpha_U}(2K_2-1)A^{I}_{\Omega_1-\Omega_2} + j2\sqrt{K_1K_2(1-K_2)\alpha_L}A^{I,B}_{\Omega_1-\Omega_2}\right]\\
&\hat{I}(2\Omega_1 - \Omega_2) = \hat{I}_{dd}(2\Omega_1 - \Omega_2) + \hat{I}_b(2\Omega_1 - \Omega_2) =\\
&= I_{dc}\sqrt{(1-K_1)\alpha_U}\left(\frac{\phi_{RF}}{4}\right)^3\sin(\phi_{dc})\left[j(2K_2-1)\sqrt{(1-K_1)\alpha_U}A^{I}_{2\Omega_1-\Omega_2} + 2\sqrt{K_1K_2(1-K_2)\alpha_L}A^{I,B}_{2\Omega_1-\Omega_2}\right],
\end{aligned}
\tag{16}
$$

where:

$$A^{I,B}_{\Omega_1-\Omega_2} = 2\left[H(\omega_o+\Omega_1-\Omega_2)-H^*(\omega_o-\Omega_1+\Omega_2)\right]\sin(\phi_{dc}/2)\cos\varphi,$$
$$A^{I,B}_{2\Omega_1-\Omega_2} = \frac{\left[H(\omega_o+2\Omega_1-\Omega_2)-H^*(\omega_o-2\Omega_1+\Omega_2)\right]}{2\sin(\phi_{dc}/2)}\cos\varphi, \quad (17)$$

and $A^{I}_{\Omega_1-\Omega_2}$ and $A^{I}_{2\Omega_1-\Omega_2}$ are the spectral coefficients, respectively, for the second- and third-order intermodulation terms for intensity modulated direct detection MWP systems, which are given in [10]. From (14) and (16) ,one can directly compute the RF powers corresponding to the fundamental term:

$$P_{RF}(\Omega_1) = 2\left|\hat{I}(\Omega_1)\right|^2 Z_{out} =$$
$$= 2I_{dc}^2 Z_{out}\alpha_U(1-K_1)\left(\frac{\phi_{RF}}{4}\right)^2\sin^2(\phi_{DC})\left|2\sqrt{K_1K_2(1-K_2)\alpha_L}A^{I,B}_{\Omega_1} - j(2K_2-1)\sqrt{\alpha_U(1-K_1)}A^{I}_{\Omega_1}\right|^2. \quad (18)$$

From Eq. 18 one can directly compute the end-to-end RF gain:

$$G_{RF}(\Omega_1) = \frac{P^{out}_{RF}(\Omega_1)}{P^{in}_{RF}(\Omega_1)} = \left[\frac{I_{dc}\pi\sin(\phi_{DC})}{2V_\pi}\frac{D}{X}\right]^2\left|jDA^{I}_{\Omega_1} + CA^{I,B}_{\Omega_1}\right|^2 Z_{in}Z_{out}, \quad (19)$$

where: $C=\sqrt{\alpha_L K_1 K_2}$, $D=\sqrt{\alpha_U(1-K_1)(1-K_2)}$, X = 1 and $Y = 2C^2/D$ for single direct detection, while $C=2\sqrt{\alpha_L K_1 K_2(1-K_2)}$, $D=(1-2K_2)\sqrt{a_U(1-K_1)}$, X = 1-2K_2 and $Y = \alpha_L K_1 X^2/D$ for balanced detection.

Regarding the noise contributions, and using the *RIN* definition, we first need to determine the value of the average current which from (13) is given by:

$$I_{dc,total} = \frac{DI_{dc}}{X}\left[(-1)^p D\left|H(\omega_o)\right|^2(1-\cos\phi_{DC}) + Y + 4C\sin\left(\frac{\phi_{DC}}{2}\right)\cos\varphi\,\mathrm{Im}\{H(\omega_o)\}\right], \quad (20)$$

where the exponent p takes the value 0 for direct detection and 1 for balanced detection. From (20) and the RIN definition we get the different contributions:

$$RIN_{\text{Thermal input}} = \frac{N^{\text{output}}_{\text{Thermal input}}}{I^2_{dc,Total}Z_{out}} = \frac{k_B T\left[\frac{\pi\sin(\phi_{DC})}{2V_\pi}\right]^2\left|jDA^{I}_{\Omega_1} + CA^{I,B}_{\Omega_1}\right|^2 Z_{in}}{\left[(-1)^p D\left|H(\omega_o)\right|^2(1-\cos\phi_{DC}) + Y + 4C\sin\left(\frac{\phi_{DC}}{2}\right)\cos\varphi\,\mathrm{Im}\{H(\omega_o)\}\right]^2}, \quad (21)$$

$$RIN_{\text{Thermal output}} = \frac{N^{\text{output}}_{\text{Thermal input}}}{I^2_{dc,Total}Z_{out}} = \frac{2k_B T}{\left(\frac{DI_{dc}}{X}\right)^2 Z_{out}\left[(-1)^p D\left|H(\omega_o)\right|^2(1-\cos\phi_{DC}) + Y + 4C\sin\left(\frac{\phi_{DC}}{2}\right)\cos\varphi\,\mathrm{Im}\{H(\omega_o)\}\right]^2}, \quad (22)$$

$$RIN_{Shot} = \frac{N_{shot}^{\text{output}}}{I_{dc,Total}^2 Z_{out}} = \frac{2e}{\left(\frac{DI_{dc}}{X}\right)\left[(-1)^p D\left|H(\omega_o)\right|^2 (1-\cos\phi_{DC}) + Y + 4C\sin\left(\frac{\phi_{DC}}{2}\right)\cos\varphi\,\mathrm{Im}\left\{H(\omega_o)\right\}\right]}, \tag{23}$$

From which RIN_{Total} can be computed:

$$\begin{aligned} RIN_{Total} = {} & \frac{k_B T\left[\frac{\pi\sin(\phi_{DC})}{2V_\pi}\right]^2 \left|jDA_{\Omega_1}^I + CA_{\Omega_1}^{I,B}\right|^2 Z_{in}}{\left[(-1)^p D\left|H(\omega_o)\right|^2 (1-\cos\phi_{DC}) + Y + 4C\sin\left(\frac{\phi_{DC}}{2}\right)\cos\varphi\,\mathrm{Im}\left\{H(\omega_o)\right\}\right]^2} + \\ & + \frac{2k_B T}{\left(\frac{DI_{dc}}{X}\right)^2 Z_{out}\left[(-1)^p D\left|H(\omega_o)\right|^2 (1-\cos\phi_{DC}) + Y + 4C\sin\left(\frac{\phi_{DC}}{2}\right)\cos\varphi\,\mathrm{Im}\left\{H(\omega_o)\right\}\right]^2} + \\ & + \frac{2e}{\left(\frac{DI_{dc}}{X}\right)\left[(-1)^p D\left|H(\omega_o)\right|^2 (1-\cos\phi_{DC}) + Y + 4C\sin\left(\frac{\phi_{DC}}{2}\right)\cos\varphi\,\mathrm{Im}\left\{H(\omega_o)\right\}\right]} + \\ & + RIN_{laser}. \end{aligned} \tag{24}$$

Finally, the optical interception points are obtained from RF powers of the intermodulation terms:

$$\begin{aligned} & P_{RF}(\Omega_1 - \Omega_2) = 2\left|\hat{I}(\Omega_1 - \Omega_2)\right|^2 Z_{out} = \\ & = 2I_{dc}^2 Z_{out}(1-K_1)\alpha_U\left(\frac{\phi_{RF}}{4}\right)^4 \left|\sqrt{(1-K_1)\alpha_U}\,(2K_2-1)A_{\Omega_1-\Omega_2}^I + j2\sqrt{K_1K_2(1-K_2)\alpha_L}\,A_{\Omega_1-\Omega_2}^{I,B}\right|^2 \\ & P_{RF}(2\Omega_1 - \Omega_2) = 2\left|\hat{I}(2\Omega_1 - \Omega_2)\right|^2 Z_{out} = \\ & = 2I_{dc}^2 Z_{out}(1-K_1)\alpha_U\left(\frac{\phi_{RF}}{4}\right)^6 \sin^2(\phi_{dc})\left|j(2K_2-1)\sqrt{(1-K_1)\alpha_U}\,A_{2\Omega_1-\Omega_2}^I + 2\sqrt{K_1K_2(1-K_2)\alpha_L}\,A_{2\Omega_1-\Omega_2}^{I,B}\right|^2. \end{aligned} \tag{25}$$

Equating them to the fundamental RF power given by (18):

$$\begin{aligned} OIP_2 &= 2\left(I_{dc}\sin^2(\phi_{DC})\frac{D}{X}\right)^2 Z_{out}\frac{\left|jDA_{\Omega_1}^I + CA_{\Omega_1}^{I,B}\right|^4}{\left|jDA_{\Omega_1-\Omega_2}^I + CA_{\Omega_1-\Omega_2}^{I,B}\right|^2}, \\ OIP_3 &= 2\left(I_{dc}\sin(\phi_{DC})\frac{D}{X}\right)^2 Z_{out}\frac{\left|jDA_{\Omega_1}^I + CA_{\Omega_1}^{I,B}\right|^3}{\left|jDA_{2\Omega_1-\Omega_2}^I - CA_{2\Omega_1-\Omega_2}^{I,B}\right|}. \end{aligned} \tag{26}$$

Acknowledgments

This research work is funded by INTEL Corporation. In addition, the authors wish to acknowledge the financial support given by the Research Excellency Award Program GVA PROMETEO II/2013/012, Spanish MINECO projects TEC2013-42332-P PIF4ESP, TEC2015-69787-REDT PIC4TB and TEC2014-60378-C2-1-R MEMES, as well as the projects FEDER UPVOV 10-3E-492 and FEDER UPVOV 08-3E-008. The work of D. Pérez was supported by the FPI-UPV Grant Program from the Universitat Politècnica de València and the work of I. Gasulla was supported by the Spanish MINECO through the Ramón y Cajal Program.